CHEMISTRY OF MATERIALS

Article

pubs.acs.org/cm

$KEu(MoO_4)_2$: Polymorphism, Structures, and Luminescent Properties

Vladimir A. Morozov,[†,‡] Alla V. Arakcheeva,[§,∥] Philip Pattison,[§,⊥] Katrien W. Meert,[#,▽] Philippe F. Smet,[#,▽] Dirk Poelman,[#,▽] Nicolas Gauquelin,[‡] Johan Verbeeck,[‡] Artem M. Abakumov,[‡] and Joke Hadermann*[,‡]

[†]Chemistry Department, Moscow State University, 119991 Moscow, Russia

[‡]EMAT, University of Antwerp, Groenenborgerlaan 171, B-2020 Antwerp, Belgium

[§]Laboratoire de Crystallographie, École Polytechnique Fédérale de Lausanne, BSP, CH-1015 Lausanne, Switzerland

[∥]Phase Solutions Ltd., CH-1012 Lausanne, Switzerland

[⊥]Swiss−Norwegian Beamline, ESRF, BP-220, F-38043 Grenoble CEDEX, France

[#]Lumilab, Department of Solid State Sciences and [▽]Center for Nano- and Biophotonics (NB-Photonics), Ghent University, 9000 Ghent, Belgium

Supporting Information

ABSTRACT: In this paper, with the example of two different polymorphs of $KEu(MoO_4)_2$, the influence of the ordering of the *A*-cations on the luminescent properties in scheelite related compounds $(A',A'')_n[(B',B'')O_4]_m$ is investigated. The polymorphs were synthesized using a solid state method. The study confirmed the existence of only two polymorphic forms at annealing temperature range 923−1203 K and ambient pressure: a low temperature anorthic α-phase and a monoclinic high temperature β-phase with an incommensurately modulated structure. The structures of both polymorphs were solved using transmission electron microscopy and refined from synchrotron powder X-ray diffraction data. The monoclinic β-$KEu(MoO_4)_2$ has a (3+1)-dimensional incommensurately modulated structure (superspace group $I2/b(\alpha\beta 0)00$, a = 5.52645(4) Å, b = 5.28277(4) Å, c = 11.73797(8) Å, γ = 91.2189(4)°, $\mathbf{q}$ = 0.56821(2)$\mathbf{a}^*$−0.12388(3)$\mathbf{b}^*$), whereas the anorthic α-phase is (3+1)-dimensional commensurately modulated (superspace group $I\bar{1}(\alpha\beta\gamma)0$, a = 5.58727(22) Å, b = 5.29188(18)Å, c = 11.7120(4) Å, α = 90.485(3)°, β = 88.074(3)°, γ = 91.0270(23)°, $\mathbf{q}$ = 1/2$\mathbf{a}^*$ + 1/2$\mathbf{c}^*$). In both cases the modulation arises due to Eu/K cation ordering at the *A* site: the formation of a 2-dimensional Eu^{3+} network is characteristic for the α-phase, while a 3-dimensional Eu^{3+}-framework is observed for the β-phase structure. The luminescent properties of $KEu(MoO_4)_2$ samples prepared under different annealing conditions were measured, and the relation between their optical properties and their structures is discussed.

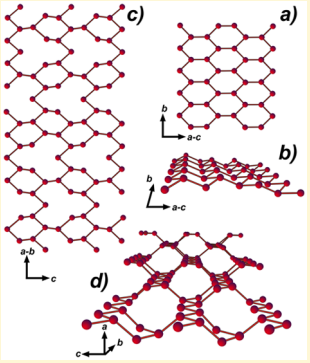

1. INTRODUCTION

White light-emitting diodes (WLEDs) are promising for replacing conventional fluorescent and incandescent lamps. They are highly reliable, have a long lifetime with low energy consumption, and are environmentally friendly.[1] Their availability can result in exciting new applications as medical and architecture lighting, portable electronics backlights, etc.[2]

Rare earth doped solid-state molybdates and tungstates exhibit outstanding chemical stability and long wavelength emission. Among these, rare earth doped scheelite-type ($CaWO_4$) molybdates and tungstates have a large potential for use in WLEDs.[3−7] Recently a new application field has emerged for these materials as thermographic phosphors, due to their capacity to accurately visualize temperature gradients with high spatial resolution.[8] Due to charge transfer from oxygen to metal, tungstate and molybdate phosphors have intense, broad absorption bands in the near-UV region. Some scheelite-type compounds, such as $PbMoO_4$, $KGd(WO_4)_2$, $NaBi(WO_4)_2$ and MWO_4 (M = Pb, Cd, Ca) are well-known and used, while other $MLn(BO_4)_2$ (M = Li, Na, K, Ag; Ln = lanthanides, B = W, Mo) materials with Eu^{3+} cations are frequently suggested as red phosphors for WLEDs. For example, $NaEu(WO_4)_2$ and $KGd_{0.75}Eu_{0.25}(MoO_4)_2$ show strong, saturated red emission.[9,10]

The scheelite-type ABO_4 ($CaWO_4$) structure is built from columns of [...- AO_8 - BO_4 - ...] directed along the *c*-axis. The AO_8 polyhedra and BO_4 tetrahedra form a 3D framework by sharing common vertices. The *A* and/or *B* cations can be partially substituted to form $(A',A'')_n[(B',B'')O_4]_m$ (A', A'' = alkali, alkaline-earth, or rare-earth elements; B', B'' = Mo, W). Such compounds are relatively simple to prepare and often have good stability and good optical properties. A large amount of vacancies can be present at the A cation site, resulting in a $(A'+A'')$:$(B'O_4+B''O_4)$ ratio different from 1:1. The substitution of Ca^{2+} cations in $CaBO_4$ (B = W, Mo) by a combination of M^+ (M = Li^+, Na^+, K^+, Ag^+) and a trivalent cation leads to the

Received: May 1, 2015
Revised: July 29, 2015
Published: July 29, 2015

DOI: 10.1021/acs.chemmater.5b01622
Chem. Mater. 2015, 27, 5519−5530

Table 1. Crystal Data, Data Collection, and Refinement of $KEu(MoO_4)_2$ Polymorphs

formula	β-$KEu(MoO_4)_2$	α-$KEu(MoO_4)_2$
formula weight (g)	510.93	
temperature (K)	293(2)	
cell setting	monoclinic	anorthic
super space group	$I2/b(\alpha\beta0)00$	$I\bar{1}(\alpha\beta\gamma)0$
lattice parameters:	5.52645(4)	5.58727(22)
a (Å)	5.28277(4)	5.29188(18)
b (Å)	11.73797(8)	11.7120(4)
c (Å)		90.485(3)
α (deg)		88.074(3)
β (deg)	91.2189(4)	91.0270(23)
γ (deg)	342.612(5)	346.03(3)
V (Å^3)	0.56821(2)**a*** − 0.12388(3)**b***	1/2**a*** + 1/2**c***
q vector		
formula units, Z	2	2
calcd density, D_x (g × cm^{-3})	4.951(8)	4.9038(4)
color	light-brown	white
Data collection		
diffractometer	MAR345	
radiation/wavelength (λ, Å)	synchrotron/0.6692	
radiation monochromator	Si(111) double crystal	
absorption coefficient, μ (mm^{-1})	12.832	12.553
F(000)	460	460
2θ range (deg)	3.002−34.298	2.000−34.708
step scan (2θ)	0.004	0.004
I_{max}	20846	20127
no. of points	7825	9346
Refinement		
refinement	Rietveld	
background function	Legendre polynomials, 16 terms	
the number of reflections (all/observed)	864/861	447/445
among them:		
main	124/124	220/218
the first-order satellites	245/245	227/227
the second-order satellites	246/244	
the third-order satellites	249/248	
no. of refined parameters/refined atomic parameters	97/69	54/30
R and R_w (%) for Bragg reflections (R_{all}/R_{obs})	1.15/1.12 and 1.43/1.40	1.50/1.49 and 2.05/2.05
among them:		
main	0.74/0.74 and 1.09/1.09	1.25/1.24 and 1.90/1.89
the first-order satellites	1.26/1.26 and 1.40/1.40	1.85/1.85 and 2.22/2.22
the second-order satellites	1.90/1.72 and 1.66/1.55	
the third-order satellites	1.57/1.52 and 1.41/1.40	
R_p and R_{wp}; R_{exp}	2.35 and 3.30; 3.32	2.96 and 4.16; 3.04
goodness of fit (ChiQ)	0.99	1.37
max./min residual density (e × Å^{-3})	0.13/−0.12	0.30/−0.26

formation of $MR(BO_4)_2$ (R = rare earth elements, Y, Bi) compounds. The existence of $MR(MoO_4)_2$ (M = Li, Na, Ag) molybdenum oxides with a scheelite-type tetragonal structure has been reported for all rare earth elements.[11−28]

$KR(MoO_4)_2$ double molybdates have a variety of crystal structures and polymorphs that can be divided in scheelite-type modifications (R = La−Dy) and non-scheelite modifications (R = Dy−Lu) with the $KY(MoO_4)_2$-type structure (space group $Pbcn$[29]). Three groups of scheelite-type modifications can be selected: 1) tetragonal (R = La−Sm) phases[30,31] or phases with a small monoclinic distortion of the scheelite subcell;[32,33] 2) phases with the incommensurate modulated structure (R = Nd,[34] Sm[35]) (superspace group $I2/b(\alpha\beta0)00$); and 3) anorthic phases with the α-$KEu(MoO_4)_2$ structure (space group $P\bar{1}$[36]).

In contrast to the tetragonal $MR(MoO_4)_2$ (M = Li^+, Na^+, K^+, Ag^+; R = Ln, Y, Bi) compounds where M^+ and R^{3+} are statistically distributed over the structure, the K^+ and Eu^{3+} cations in α-$KEu(MoO_4)_2$ are ordered. Among the incommensurately modulated structures, the A site cations are completely ordered in $KNd(MoO_4)_2$,[34] while they are only partially ordered in $KSm(MoO_4)_2$.[35] It should be noted that the data about the number of polymorph modifications for $KEu(MoO_4)_2$ are contradictory. Klevtsov et al.[37] selected five modifications of $KEu(MoO_4)_2$ (anorthic α-phase → monoclinic β-phase with the α- $KSm(MoO_4)_2$-type structure (IM structure[37]) × monoclinic β'-phase with α-$KBi(MoO_4)_2$-type structure (unknown structure) → orthorhombic γ-phase with the $KY(MoO_4)_2$-type structure → δ-phase (unknown struc-

DOI: 10.1021/acs.chemmater.5b01622
Chem. Mater. 2015, 27, 5519−5530

ture) with increasing temperature, while other authors only discussed anorthic α- and monoclinic β-modifications (β'-phase in accordance with Klevtsov et al.[37]). According to Klevtsov et al.[37] the pure orthorhombic γ-phase with the $KY(MoO_4)_2$-type structure can be synthesized by annealing at 1123 K followed by quenching to room temperature. β'-$KEu(MoO_4)_2$ was grown from the melt, and the crystal structure of this phase was described as monoclinic[36,38−40] but not specified in detail. It should be noted that different authors have indexed the X-ray powder diffraction (XRPD) patterns with different unit cell parameters.[36,38,39] Comparison of data from different authors is difficult because XRPD patterns are almost absent in the papers.[35] Using the structural data obtained for $KNd(MoO_4)_2$, we have shown that all reflections listed in JCPDS PDF2 No. 31-1006 for the monoclinic (β-phase in accordance with Klevtsov et al.[37]) β- $KEu(MoO_4)_2$ can be indexed successfully using the unit cell parameters a = 5.5241(17) Å, b = 5.2864(15) Å, c = 11.713(3) Å, γ = 91.247(17)°, and $\mathbf{q}$ = 0.5641(2)$\mathbf{a}^*$ − 0.1335(4)$\mathbf{b}^*$ in the monoclinic superspace group, $I2/b(\alpha\beta0)00$.[34]

C. Guo et al.[13] studied the influence of the calcination temperature from 823 to 1173 K on the luminescent properties of $KEu(MoO_4)_2$ and showed that the anorthic α-$KEu(MoO_4)_2$ structure does not change by increasing the calcination temperature from 823 to 973 K. According to C. Guo et al., XRPD patterns of $KEu(MoO_4)_2$ samples prepared at calcination temperatures above 1073 K are in agreement with the JCPDS PDF2 No. 32-0782. It was found that the intensity of the red emission line peaking at 616 nm owing to the electric dipole transition $^5D_0 \rightarrow {}^7F_2$ for $KEu(MoO_4)_2$ increases with increasing sintering temperature and reaches a maximum at 1073 K. Thus, the luminescent intensity of monoclinic $KEu(MoO_4)_2$ is stronger than that of the phosphors with an anorthic structure. The intensities of the phosphors decrease as the processing temperature increases up to 1173 K.[13] It should be noted that the authors completely ignore the presence of small intensity reflections over the 2θ range 10−20° on the XRPD patterns of the $KEu(MoO_4)_2$ samples prepared at calcination temperatures above 1073 K. These small intensity reflections were not listed in JCPDS PDF2 No. 32-0782 for $KEu(MoO_4)_2$, but they are clearly observed on the XRPD patterns. The high luminescent intensity for the sample prepared at 1073 K can result from a small amount of $KEu(MoO_4)_2$ phase with an incommensurately modulated scheelite-type structure.

The aim of the present paper is to reveal the relation between the luminescent properties and structure for different modifications of $KEu(MoO_4)_2$.

2. EXPERIMENTAL SECTION

2.1. Materials and Sample Preparation. The low-temperature (LT) α-modification of $KEu(MoO_4)_2$ was prepared from a (1:1:4) stoichiometric mixture of K_2CO_3 (99.99%), Eu_2O_3 (99.99%), and MoO_3 (99.99%), by a routine ceramic technique in a Pt crucible at 923 ± 10 K for 30 h in air followed by slow cooling in the furnace from 923 K to room temperature (T_R). α-$KEu(MoO_4)_2$ was annealed at different temperatures (973, 1023, 1073, 1123, 1173, and 1203 K) for 12 h and cooled under different cooling conditions (slow cooling from the annealing temperature to T_R, quenching from the annealing temperature to liquid nitrogen (N_2)) to solve the unclear problem with the number of polymorph modifications (Table S1). The high-temperature (HT) β-$KEu(MoO_4)_2$ was synthesized from the α-phase by annealing at 1203 ± 10 K for 10 h in air followed by quick quenching from the high temperature to liquid nitrogen temperature.

2.2. Characterization. Powder X-ray diffraction (PXRD) patterns were collected on a Huber G670 Guinier diffractometer ($CuK_{\alpha1}$ radiation, λ = 1.5406 Å, curved Ge(111) monochromator, transmission geometry, image plate detector) for the determination of the unit cell parameters. PXRD data were collected at room temperature over the 4°−100° 2θ range with steps of 0.005°. To determine the unit cell parameters, the PXRD data were refined by Le Bail decomposition[41] using the JANA2006 software.[42,43]

For the transmission electron microscopy study, the samples were made by crushing the powder in an agate mortar and dispersing the crushed powder in methanol. Several drops of this solution were deposited on a copper grid covered with a holey carbon film. Selected area electron diffraction (SAED) patterns were obtained using a Philips CM20 transmission electron microscope operated at 200 kV, equipped with a CCD camera. The elemental composition of the samples was confirmed by energy dispersive X-ray (EDX) analysis performed with a Philips CM20 microscope with an Oxford INCA attachment. For the EDX analysis, the results were based on the K_K, Eu_L, and Mo_L lines.

High resolution high angle annular dark field scanning transmission electron microscopy (HAADF-STEM) images were obtained on a FEI Titan 60-300 transmission electron microscope equipped with a probe aberration corrector, operated at 300 kV.

The synchrotron X-ray powder diffraction (SXPD) data were collected at the BM01A beamline (Swiss-Norwegian Beamline) of the European Synchrotron Radiation Facility (ESRF, Grenoble, France). A wavelength of 0.6692 Å was selected using a Si(111) double crystal monochromator, and the synchrotron beam was focused on a spot size of 0.3 mm × 0.3 mm using a combination of curved mirrors and sagittal bent second crystal. The sample was put into a borosilicate capillary of 0.5 mm diameter, and the data were collected at room temperature. A Mar345 image plate detector was used to register the powder patterns. The sample-to-detector distance of 250 mm was calibrated using a LaB_6 reference powder. Exposure times per sample were typically 30 s per image, and the samples were rotated during data collection at a speed of 1° s^{-1}. Exposure times were chosen to avoid any pixel saturation. Details of experiments and characteristics of the final structure refinements are listed in Table 1. Rietveld analysis of the incommensurately modulated structure was performed using the JANA2006 program package.[42,43] Illustrations were produced with this package in combination with the program DIAMOND.[44]

Electron Energy Loss Spectroscopy (EELS) was performed on a monochromated Titan 80-300 microscope operated at 80 keV to reduce knock-on damage with an energy resolution of 100 meV. Data were acquired with a 0.01 eV/pixel dispersion and a 0.2 ms exposure time in thin areas of the sample to avoid multiple scattering to alter the results. The tail of the Zero-Loss was removed by subtraction of a second-order polynomial background fit.

Luminescent emission and excitation spectra were recorded on an Edinburgh Instruments FS920 fluorescence spectrometer with a monochromated 450W Xe arc as the excitation source. Decay profiles were collected using an Andor intensified CCD (Andor DH720) connected to a 500 mm spectrograph, combined with a dye laser as excitation source. Temperature dependent measurements were performed using an Oxford Optistat CF cryostat.

3. RESULTS AND DISCUSSION

3.1. Elemental Composition. The composition of both $KEu(MoO_4)_2$ modifications was verified using EDX analysis at 4 points for 10 different crystallites of which also electron diffraction patterns were taken. The compositions were found to be 24.5(2) at.% K: 25.3(4) at.% Eu: 50.2(4) at.% Mo and 24.7(7) at.% K: 25.1(1) at.% Eu: 50.2(7) at.% Mo for the β- and α-modification, respectively. This is close to the nominal $KEu(MoO_4)_2$ composition.

3.2. Preliminary Characterization. PXRD patterns of α-$KEu(MoO_4)_2$ and the samples prepared from the α-phase under different annealing and cooling conditions are shown in

DOI: 10.1021/acs.chemmater.5b01622
Chem. Mater. 2015, 27, 5519−5530

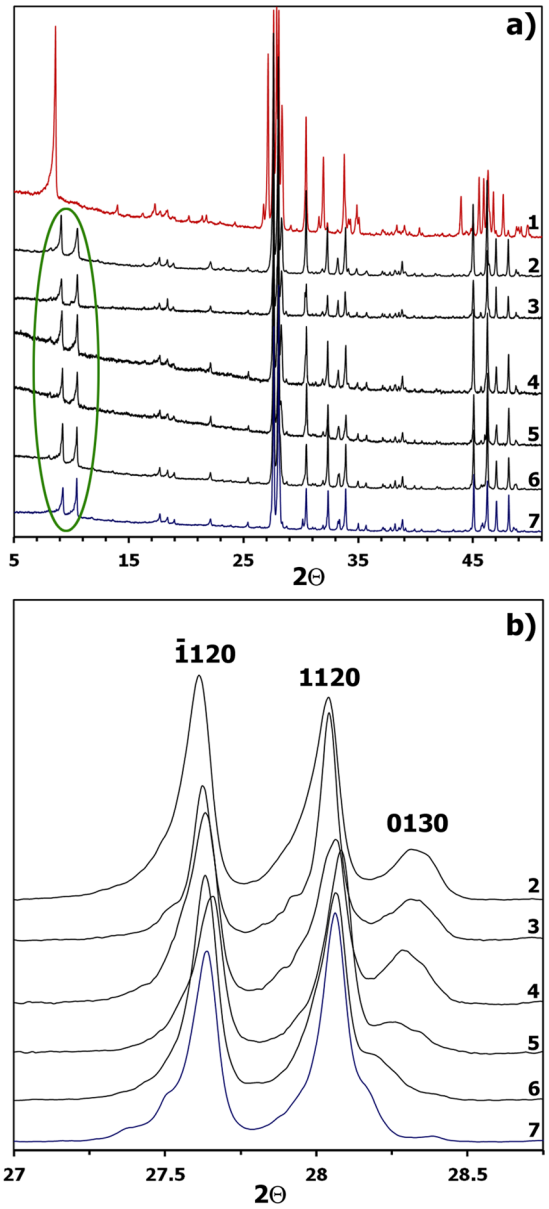

Figure 1. Part of the PXRD patterns of the $KEu(MoO_4)_2$ samples prepared from α-$KEu(MoO_4)_2$ (1) by annealing at 973 K (2), 1023 K (3), 1073 K (4), 1123 K (5), 1173 K (6), and at 1203 ± 10 K followed by fast quenching from the high temperature to liquid nitrogen (β-$KEu(MoO_4)_2$ (7)) in 2θ ranges of 5−51° (a) and 27−28.75° (b).

Figure 1. All reflections of the PXRD pattern of the α-phase correspond to the anorthic structure (space group $P\bar{1}$[36]) with unit cell parameters refined by Le Bail decomposition: a = 11.1869(2) Å, b = 5.30038(6) Å, c = 6.93707(8) Å, α = 112.4276(8)°, β = 111.5964(9)°, γ = 90.9988(9)°. PXRD patterns of other samples prepared from the α-phase differ insignificantly (Figure 1). The main feature of all PXRD patterns of these samples is the presence of two fairly intense reflections in the 8°−11° 2θ range (shown in the green ellipse in Figure 1a). Earlier similar reflections were observed on PXRD patterns of $KR(MoO_4)_2$ (R = Nd,[34] Sm[35]) with incommensurately modulated structures and indexed as 0001 and $101\bar{1}$, respectively. The positions of these satellite reflections on PXRD patterns are almost independent of the heating and cooling conditions, while the positions of the basic reflections change significantly (Figure 1b). The unit cell parameters were refined by Le Bail decomposition using the data of the incommensurately modulated $KNd(MoO_4)_2$ crystal structure as initial parameters. The unit cell parameters determined by Le Bail decomposition from the PXRD patterns are given in Table S1. According to Table S1 and Figure 1 the $\alpha \rightarrow \beta$ phase transition is not reversible. Thus, PXRD studies do not show any orthorhombic γ-$KEu(MoO_4)_2$ phase with the $KY(MoO_4)_2$-type structure but show the existence of only two modifications for $KEu(MoO_4)_2$: an anorthic α-phase and a monoclinic β-modification with incommensurate modulated structure.

3.3. Electron Diffraction Study. *HT β-Phase.* $[001]^*_\beta$, $[100]^*_\beta$, and $[1\bar{1}0]^*_\beta$ ED patterns of β-$KEu(MoO_4)_2$ (Figure 2) show a high likeness with those of $KR(MoO_4)_2$ (R = Nd,[17]

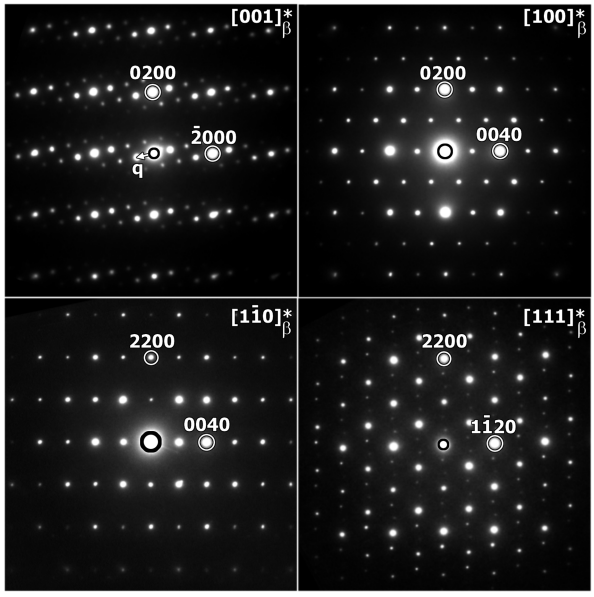

Figure 2. ED patterns along the main zone axes for the monoclinic β-$KEu(MoO_4)_2$.

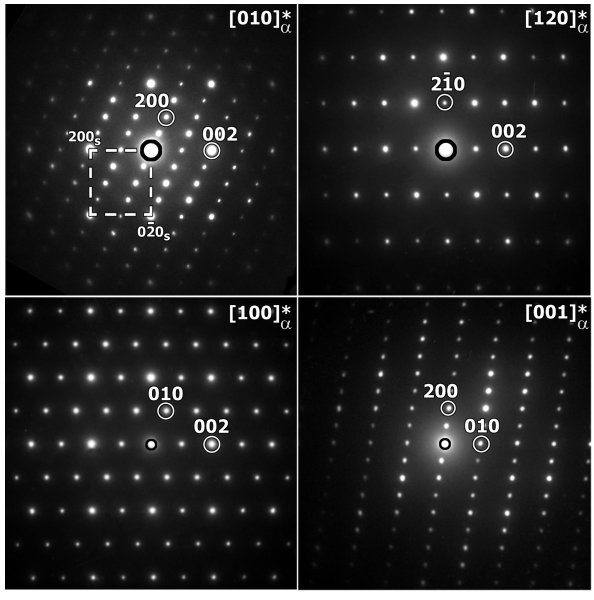

Figure 3. ED patterns along the main zone axes for the anorthic α-$KEu(MoO_4)_2$.

DOI: 10.1021/acs.chemmater.5b01622
Chem. Mater. 2015, 27, 5519−5530

Sm[18]), which have a (3+1)D incommensurately modulated structure. The reflections in the $[1\bar{1}0]^*_\beta$ and $[100]^*_\beta$ ED patterns all correspond to the tetragonal scheelite subcell with parameters $a_s \approx 5.46$ Å, $c_s \approx 11.86$ Å (s refers to the scheelite-type unit cell) and thus are considered main reflections. However, next to main reflections, low intensity reflections are observed in the other ED patterns, $[001]^*_\beta$ and $[111]^*_\beta$. These are satellite reflections that need four $hklm$ integers to be indexed, corresponding to $\mathbf{H} = h\mathbf{a}^* + k\mathbf{b}^* + l\mathbf{c}^* + m\mathbf{q}$, with modulation vector $\mathbf{q} \approx 0.57\mathbf{a}_s^* - 0.122\mathbf{b}_s^*$ and $m \neq 0$. The $m = 0$ reflections are the main reflections. The values of the $\mathbf{q}$ vector components cannot be expressed as rational values and therefore designate the structure as incommensurately modulated. The reflection conditions $hklm$: $h + k + l = 2n$ and $hk0m$: $h, k = 2n$ correspond to the (3+1)D superspace group $I2/b(\alpha\beta0)00$ (unique axis c) (15.1.4.1 in Stokes-Campbell-van Smaalen notations, $B2/b(\alpha\beta0)00$ in a standard setting).[45] The $[1\bar{1}0]^*$ pattern shows $hk00$: $h, k = 2n+1$ reflections that are forbidden by the $I2/b$ symmetry. However, on tilting the sample around the $[hk00]$ direction, these reflections become weaker and finally disappear in the $[001]^*$ pattern. Therefore, these reflections are due to double diffraction, not violating the $I2/b$ symmetry.

LT α-Phase. $[010]^*_\alpha$, $[100]^*_\alpha$, $[120]^*_\alpha$, and $[001]^*_\alpha$ ED patterns of α-$KEu(MoO_4)_2$ are shown in Figure 3. They can be indexed using the space group $P\bar{1}$ with the unit-cell parameters refined from the PXRD pattern. The relation between the unit-cell vectors of the monoclinic (β-phase) and the anorthic unit cell (α-phase) is as follows: $[010]^*_\alpha = [001]^*_\beta$, $[100]^*_\alpha = [100]^*_\beta$, and $[120]^*_\alpha = [1\bar{1}0]^*_\beta$. The difference between the β-phase and the α-phase is clearly observed when comparing the $[010]^*_\alpha$ and $[001]^*_\beta$ ED patterns, whereas the $[100]^*_\alpha$ and $[120]^*_\alpha$ differ only slightly from $[100]^*_\beta$ and $[1\bar{1}0]^*_\beta$, respectively.

3.4. Refinement of the $KEu(MoO_4)_2$ Crystal Structures.

HT β-Phase. The SXPD data were collected in the 2θ range of 3.002−34.298° with steps of 0.004°. The structure was refined against the SXPD data in the scheelite-type setting with superspace group $I2/b(\alpha\beta0)00$. The cell parameters and $\mathbf{q}$ vector from electron microscopy were used as input and refined as $a = 5.52645(4)$ Å, $b = 5.28277(4)$ Å, $c = 11.73797(8)$ Å, $\gamma = 91.2189(4)°$, $\mathbf{q} \approx 0.568\boldsymbol{a}^* - 0.1239\boldsymbol{b}^*$. Refining the unit cell and profile parameters together allowed to index 864 of the main reflections and up to third-order satellite reflections (Table 1 and Figure 4). In the lower-angle range ($3° \leq 2\theta \leq 11.6°$), the first-order satellites are the strongest reflections and also the third-order satellites are clearly present, whereas of the main reflections only three weak ones are present (Figure 4).

For the initial parameters of the refinement, the Mo and O atomic parameters of $KNd(MoO_4)_2$[34] were used, including the displacive modulation function's first-order Fourier amplitudes, completed by K and Eu occupying the A position statistically ($x_1 = 0.5$, $x_2 = 0.25$, $x_3 = 0.88$). The displacive modulation functions, atomic coordinates, and isotropic atomic displacement parameters were subsequently refined. According to the $KNd(MoO_4)_2$[34] model of the occupation modulation in the A site, two Crenel functions (Figure S2 of the Supporting Information) were chosen for the K and Eu atomic domains with parameters $x_4^0 = 0$ (K) and $x_4^0 = 0.5$ (Eu) and an occupation parameter $o = 0.5$ for both A atoms (crenel-I model). The occupation parameters were fixed to satisfy the EDX results. Acceptable values of R were obtained for the main reflections and higher R values for satellite reflections. The calculated electron and residual electron density near the $A = (K_{0.5}Eu_{0.5})$ position showed that the assumption of an average half occupation along the internal axis x_4 by both K and Eu was not correct.

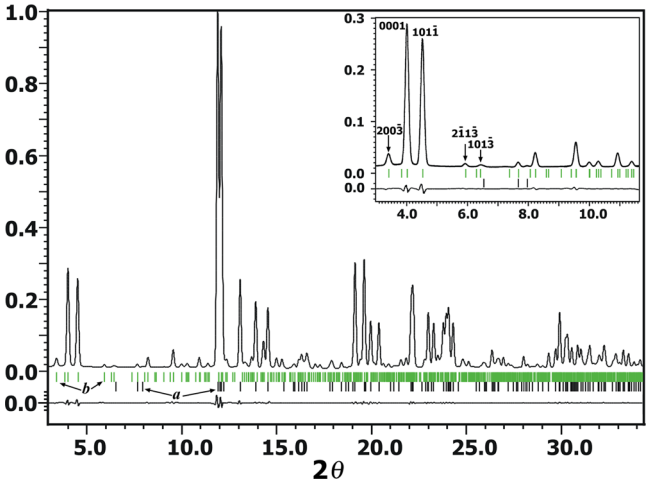

Figure 4. Experimental, calculated, and difference SXPD patterns for β-$KEu(MoO_4)_2$. Tick marks denote the peak positions of possible Bragg reflections for (a) the main reflections and (b) satellites. The inset shows a part of the profile with the indexation of some reflections. The pair of strong low-angle satellites is a characteristic feature of the scheelite-like incommensurate structures.

The crenel-I model was improved by refining the occupation parameters to $o[K1] = 0.9851(1)$ and $o[Eu2] = 0.015(1)$ ($0 < t < 0.5$) and $o[Eu1] = 0.985(1)$ and $o[K2] = 0.015(1)$ ($0.5 < t < 1$) (crenel-II model). The coordinates (x, y, z), ADPs, and displacive modulations of K1 and K2 and of Eu1 and Eu2 were fixed to be equal, and further restraints $o[K1] = o[Eu1] = 1 - o[Eu2]$, $o[Eu2] = o[K2]$ were used. Overall only $o[Eu1]$ was included as an additional refined parameter compared to the crenel-I model. Two harmonic terms were included in the displacive modulations for the Eu/K cations, three for the Mo and O atoms.

The crenel-II model was successfully refined using isotropic atomic displacement parameters (ADP). The sufficiently large ratio between observed reflections and atomic refined parameters (864/69 > 8.9) allowed the refinement of the anisotropic ADP for K, Eu, and Mo cations. The reliability factors $R_{all} = 1.15\%$, $R_p = 2.35\%$ showed that the experimental and calculated profile agree well. Table 1 shows further numerical data on the data collection and refinement. Tables S2 and S3 of the Supporting Information list the atomic coordinates, crystallographic parameters, modulation parameters, and interatomic distances for β-$KEu(MoO_4)_2$. Figure 4 shows the experimental, calculated, and difference XRD patterns.

LT α-Phase. The SXPD data were collected in the 2θ range of 2.000−34.708° with steps of 0.004°. In accordance with Klevtsova et al.[36] and our PXRD and ED study, the α-$KEu(MoO_4)_2$ has the anorthic scheelite-type structure (space group $P\bar{1}$) but can also be considered in the scheelite-type settings as a commensurately modulated structure with the anorthic superspace group $I\bar{1}(\alpha\beta\gamma)0$ and the modulation vector $\mathbf{q} = 1/2\boldsymbol{a}_s^* + 0\boldsymbol{b}_s^* + 1/2\boldsymbol{c}_s^*$. [The transformation matrix from the commensurately modulated subcell (s) to the anorthic supercell

DOI: 10.1021/acs.chemmater.5b01622
Chem. Mater. 2015, 27, 5519−5530

$$(P\bar{1})\ \text{is}\ T = \begin{pmatrix} 2 & 0 & 0 \\ 0 & 1 & 0 \\ -1/2 & 0 & 1/2 \end{pmatrix}$$

in the matrix equation $A_P\bar{1} = A_s{}^*T$.] The fractional atomic coordinates of $CaWO_4$ were used as the initial parameters for the refinement of the average structure after their transformation from space group $I4_1/a$ to $I\bar{1}$. According to the analysis of the residual electron density maps, two Crenel functions were applied for the K and Eu atoms with occupation parameter $o = 0.5$ for both A atoms, Eu $x_4{}^0 = 0$ and K $x_4{}^0 = 0.5$. The occupation parameters were fixed in agreement with the EDX results. The displacive modulations were approximated with one harmonic term for the Eu, K, Mo, and O atoms. The structure has been refined as commensurately modulated with $t_0 = 1/4$.

The reliability factors $R_{all} = 1.53\%$, $R_p = 2.96\%$ indicate that the experimental and calculated profiles agree well. Table 1 lists further data on the refinement. Tables S4–S5 lists the atomic coordinates, crystallographic parameters, modulation parameters, and interatomic distances of α-$KEu(MoO_4)_2$. Figure 6 shows the experimental, calculated, and difference SXRD patterns.

3.5. Specific Features of the $KEu(MoO_4)_2$ Crystal Structures. The incommensurately modulated scheelite-type β-phase has strong satellite reflections on the X-ray diffraction patterns, some even stronger than many main reflections (Figure 4), with also strong reflections at low angles (inset Figure 4). These features are characteristic for the incommensurately modulated scheelite-type β-phases.

The scheelite-type ABO_4 ($CaWO_4$) structure exists of [...-AO_8 - BO_4- ...] columns oriented along the c-axis. For the A positions, many different distributions of cations have been reported, ordered, and disordered and with positions fully or partially occupied, whereas the B positions were always fully occupied and topologically identical. The K and Eu cation ordering in the β-phase is demonstrated in Figure 5, showing the $9a \times 8.5b \times 1c$ representative portion of the structure. The distribution of K and Eu in the A position is aperiodic in the ab plane and periodic along the c axis (Figure 5). The ionic charge and radius of K and Eu cations, as well as their electronic structure and covalent bonding preferences are different, and therefore a different first coordination sphere environment is required. The A-O distances are more spread along the internal coordinate t for the K–O values than for the Eu–O values (Figure S3). The data in Table S4 of the Supporting Information reflect that two distortion modes with either stretching of the Mo–O bonds (1.92–1.70 Å) or bending of the O–Mo–O bond angles (~132–93°) are active, similar to the situation observed in other incommensurately modulated cation-ordered scheelite-type structures.[46]

The structure of β-$KEu(MoO_4)_2$ can, like other scheelite-type compounds, be described as columns along the c-axis consisting of A cations and MoO_4 (Figure 5). Each column consists of either $\{KMoO_4\}$ or $\{EuMoO_4\}$ units. As a result, it can be clearly seen in the ab projection that the K and Eu distribution over the structure follows an incommensurate compositional modulation wave propagating in the direction of vector $\mathbf{q} = \alpha\mathbf{a}^* + \beta\mathbf{b}^*$. Four $\{KMoO_4\}$ or $\{EuMoO_4\}$ columns form 4-membered blocks grouped into "dimers" and "trimers" (respectively indicated in orange and yellow in Figure 5) along the [010] direction of the scheelite subcell. Aperiodic

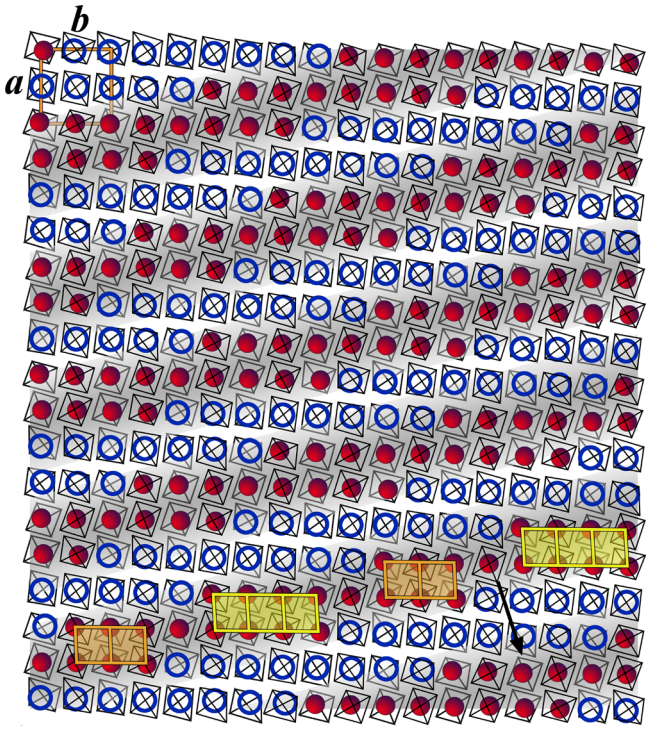

Figure 5. A portion of the β-$KEu(MoO_4)_2$ aperiodic structure in the ab projection. The red balls and blue rings indicate Eu and K positions, respectively. The $[MoO_4]$ tetrahedra are represented by their edges. The gray-and-white wave indicates the continuously changing chemical composition from mainly $\{Eu[MoO_4]\}$ (center of the gray part) to mainly $\{K[MoO_4]\}$ (center of the white part). The direction and length of this wave (arrow) is parallel to the **q** vector with length $1/|\mathbf{q}|$. The dimers (marked in orange) and trimers (marked in yellow) of the $\{EuMoO_4\}$ columns are marked.

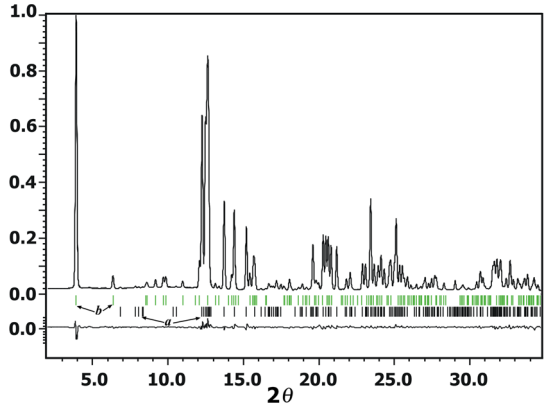

Figure 6. Experimental, calculated, and difference SXPD patterns for α-$KEu(MoO_4)_2$. Tick marks denote the peak positions of possible Bragg reflections for (a) the main reflections and (b) satellites.

alternation of the "dimers" and "trimers" can be considered as the origin of the incommensurability in the β-phase.

The ac projections of the crystal structure are shown in Figure 7 for the two $KEu(MoO_4)_2$ modifications. The difference between them lies in the ordering of the cations in the A-sublattice of the scheelite-type structure, clearly observed in these projections. The difference and similarity between the structures can be better understood if we consider the mutual arrangement of Eu^{3+} and the geometry of their surroundings by neighboring Eu^{3+} cations.

DOI: 10.1021/acs.chemmater.5b01622
Chem. Mater. 2015, 27, 5519–5530

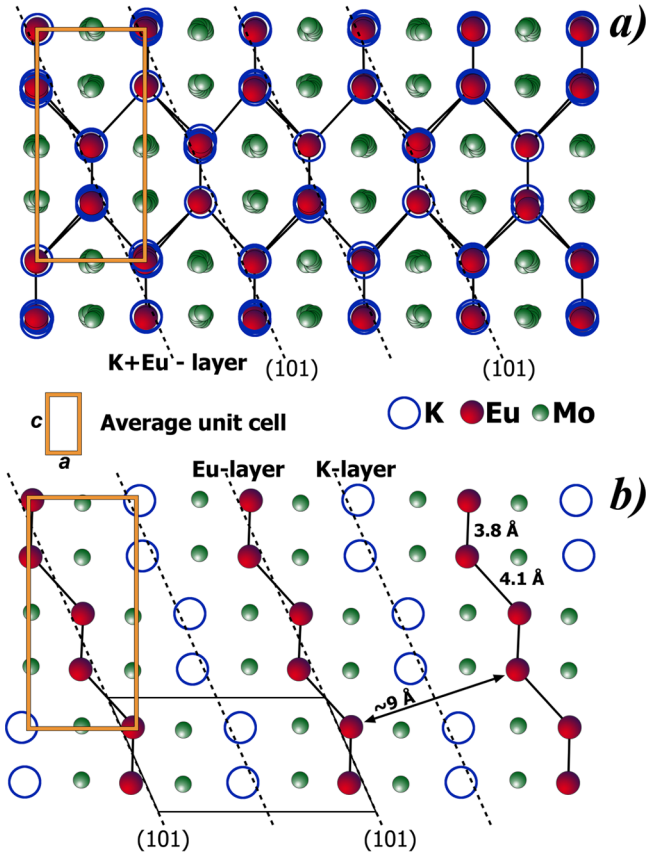

Figure 7. The *ac* projection of the crystal structure for the two $KEu(MoO_4)_2$ modifications (only K, Eu, and Mo cations are shown for simplicity): β- (a) and α- (b).

In the α-phase, the ordering of the Eu^{3+} and K^+ cations leads to the formation of similar zigzag Eu^{3+}- and K^+-layers, which are confined to the (101) plane and alternate along the [100] direction of the scheelite-type unit cell (Figure 7b). Two neighboring Eu^{3+}-layers are separated by a similar zigzag K^+-layer. The shortest distance between two nearest Eu^{3+} cations is equal to 9 Å between layers, and it varies from 3.889(7) Å to 3.981(7) Å within the layer (Table S6 of the Supporting Information). Six Eu^{3+} cations form six-membered rings (Figure 8a), and a Eu^{3+}-layer can be represented as constructed from these rings (Figure 8b). Thus, the cation ordering in the α-phase leads to the formation of a 2D Eu^{3+} network. In the β-phase, similar six-membered Eu^{3+}-rings can be selected (Figure 8c) with Eu^{3+}–Eu^{3+} distances between 3.83(7) Å and 4.20(9) Å (Table S4 of the Supporting Information). However, unlike in the α-phase, these rings form a 3D Eu^{3+} framework (Figure 8d).

In a previous paper, we summarized the crystal structure data for all $(A',A'')_{1-x}BO_4$ (B = Mo, W) scheelites, showing that the ordering of the A-site cations depends on the difference in their ionic radii r(A')-r(A'') and on the amount of cation vacancies x.[46] Like other $NaR(MoO_4)_2$ (R = rare earth elements) molybdenum oxides, $NaEu(MoO_4)_2$[47,48] has only the tetragonal scheelite-type structure with a statistical distribution of M^+ and R^{3+}. $KR(MoO_4)_2$ (R = La3[30,31]-Ce[49]) has similar statistical distribution of K^+ and R^{3+}. Increasing the r(K)-r(R) difference from 0.367 Å (Ce) to 0.401 Å (Nd) turns the K^+ and R^{3+} distribution into an ordered one, forming the incommensurately modulated structures (R = Nd–Eu). Up to R = Dy, anorthic scheelite-type phases with the α-$KEu(MoO_4)_2$ structure are formed.[50] Increasing the r(K)-r(R) difference further, from 0.483 Å (Dy) to 0.491 Å (Y) results in phases with the nonscheelite $KY(MoO_4)_2$-type structure. Thus, the scheelite-type structure is apparently restricted to r(A')-r(A'') values below 0.49 Å.

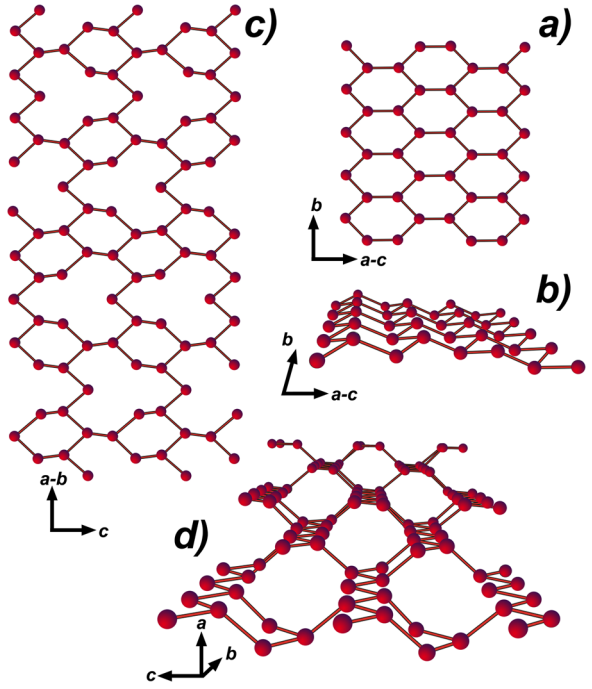

Figure 8. Eu-layers in α- (a,b) and β-$KEu(MoO_4)_2$ (c,d) structures.

3.6. HAADF-STEM Observations. The HAADF-STEM image of β-$KEu(MoO_4)_2$ along the most informative zone axis [001] is presented in Figure 9, the bright dots corresponding to the projected cationic columns. The A (K or Eu) and B (Mo) cations project onto each other along this direction. The

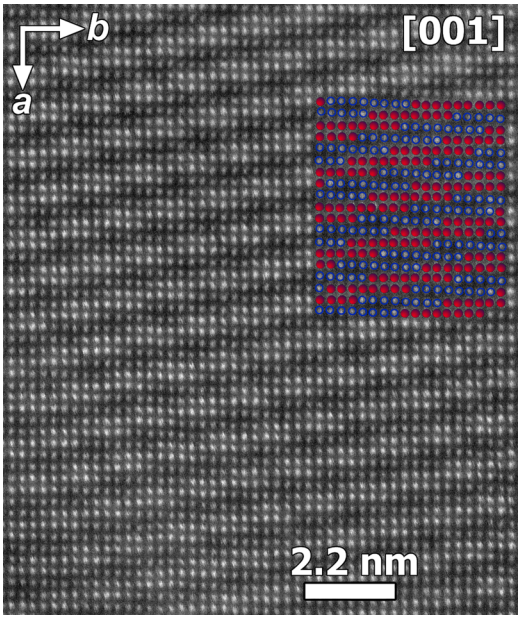

Figure 9. [001] HAADF-STEM image of β-$K_{0.5}Eu_{0.5}MoO_4$ and the structural model (only K and Eu cations are shown for simplicity) overlay on the experimental HAADF-STEM image (bottom). Red balls are Eu positions, blue rings are K positions.

DOI: 10.1021/acs.chemmater.5b01622
Chem. Mater. 2015, 27, 5519–5530

brightness of the dots on HAADF-STEM images is related to the average Z of the whole projected atomic column (Z_{Eu} = 63; Z_K = 19; Z_{Mo} = 42). The average Z of oxygen columns is low relative to that of cation columns, which makes the oxygen columns invisible on the image. The brighter bands correspond to the Eu/Mo layers. The HAADF-STEM image shows that the β-phase is (3+1)-dimensionally modulated. The brightness of the dots on the image varies due to the compositional modulation, showing a wavy contrast; the periodicity and orientation of the variation agree with the modulation vector seen on the ED patterns.

3.7. Luminescent Properties. The luminescent properties were measured for four different samples: the low temperature α-phase, the samples annealed at 973 and 1173 K, and the high temperature β-phase. In Figure 10, the excitation (λ_{em} = 615 nm) and emission (λ_{ex} = 395 nm) spectra are shown, and the characteristic 4f-4f transitions of Eu^{3+} dominate in both spectra. In the excitation spectrum an additional dual broad band can be observed in the short wavelength region. These broad features are in general linked to host related mechanisms like charge transfer states and point to an energy transfer between the host and the luminescent ion. Apparently, the annealing temperature has an influence on the efficiency of this energy transfer. The excitation spectrum of the β-phase exhibits the highest contribution of the charge transfer band and thus the most efficient energy transfer mechanism between the host and the luminescent ion as compared to direct excitation. For all samples, the majority of the emission can be ascribed to the $^5D_0 - {}^7F_2$ forced electric dipole transition at around 615 nm, indicating that the site symmetry of the A position, and thus the position of the Eu^{3+} ion, possesses no inversion center.[51] This confirms the relatively low site symmetry as established by the structural data. Typically, the local environment of the Eu^{3+} ions has only a minor influence on the spectra and differences are limited to small shifts in energy levels and thus in the positions of the transitions in the spectra; therefore, measurements at low temperature are needed to avoid thermally induced peak broadening. Figure 11, measured at a temperature of 10 K, reveals small differences in the emission from the $^5D_0$ level for the studied samples. In all materials, the $^5D_0 - {}^7F_0$ transition is well separated from the three peaks of the $^5D_0 - {}^7F_1$ transition between 590 and 600 nm. For the α-phase, the $^5D_0 - {}^7F_0$ transition is observed at 579.5 nm, but it is shifted to 579 nm for the annealed and the high temperature β-phase samples. Apparently, the $^5D_0$ level shifts 2 meV to higher energies after annealing the samples. The annealing induces also changes in the $^7F_2$ multiplet splitting, as reflected in the $^5D_0 - {}^7F_2$ transition (Figure 11(bottom)). However, calculating the barycenter energy for the $^7F_2$ level (i.e., in the absence of crystal field splitting) is not possible with sufficient precision due to the involvement of multiple overlapping energy levels.

The inset of Figure 10 shows that, in addition to the above differences between the samples, the fraction of emission coming from the higher lying $^5D_2$ and $^5D_1$ levels is relatively much more prominent for the high temperature β-phase as compared to the other modifications. In general, the non-radiative depopulation of the higher lying ^5D_J levels to the $^5D_0$ level can occur by two mechanisms, cross-relaxation and multiphonon relaxation. Cross-relaxation between two neigh-

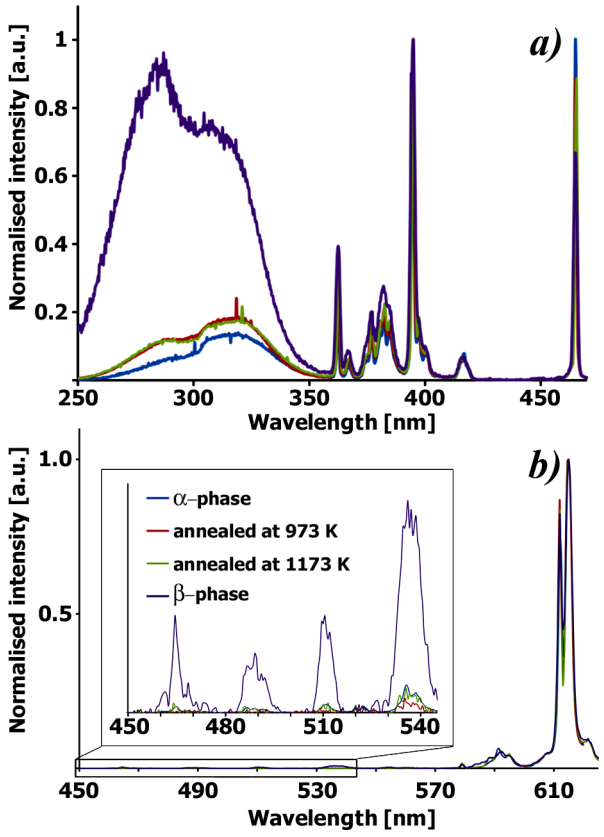

Figure 10. Excitation (a) (λ_{em} = 615 nm) and emission (b) (λ_{ex} = 395 nm) spectra of four $KEu(MoO_4)_2$ samples at room temperature. The inset shows the emission of the $^5D_1$ and $^5D_2$ level normalized to the peak of the emission of the $^5D_0$ level for all samples at room temperature.

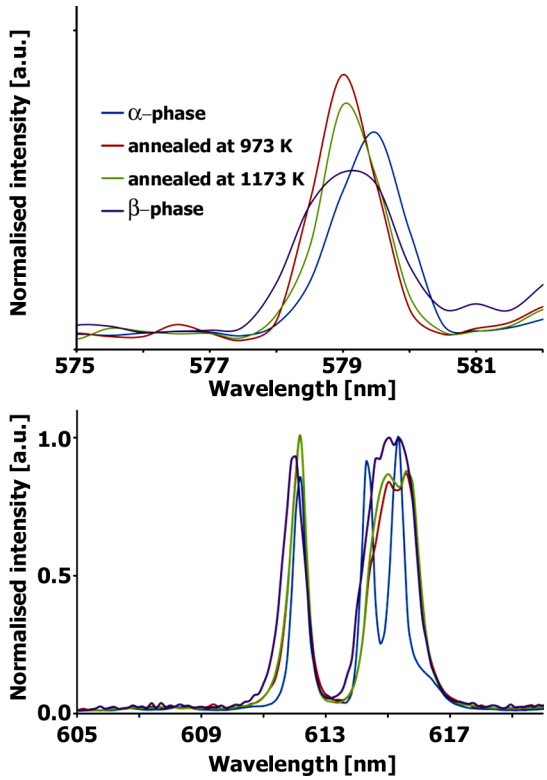

Figure 11. Emission (λ_{ex} = 395 nm) of the $^5D_0$ level at 10 K: $^5D_0 - {}^7F_0$ (up) and $^5D_0 - {}^7F_2$ (down) transitions.

DOI: 10.1021/acs.chemmater.5b01622
Chem. Mater. 2015, 27, 5519−5530

boring ions involves an energy transfer of the $^5D_1 - {}^5D_0$ energy difference from one ion to the other. A relatively small distance between the luminescent ions is necessary for this transfer process to occur, and thus a (locally) high Eu^{3+} concentration is needed. A second way of depopulating higher lying energy levels in ions is by multiphonon relaxation. In this case the energy of the phonons should be resonant with the energy difference between the higher and the lower lying level.

In order to gain more insight in the involved mechanisms, time-resolved measurements were performed. In Figure 12 the

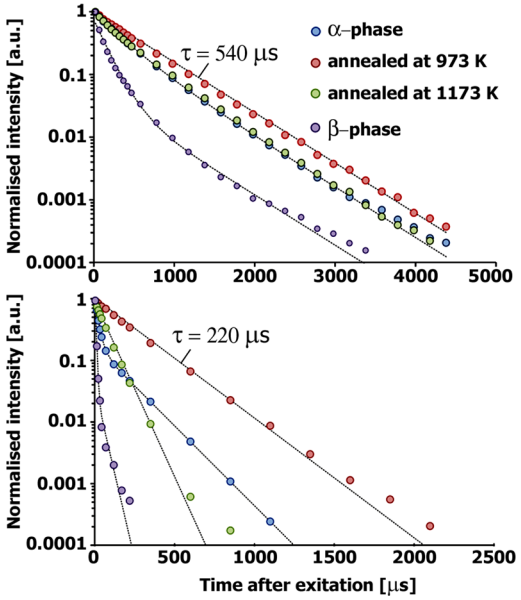

Figure 12. Decay profiles of the $^5D_0$ − emission (λ_{exc} = 337 nm) at 10 K (up) and at room temperature (down). The dashed lines are exponential fits.

decay profiles (λ_{exc} = 337 nm) of the $^5D_0$ − emission of all the samples both at 10 K and at T_R are shown to be very different. The modulated monoclinic sample annealed at 973 K shows a monoexponential decay and fitting the expression $I(t) = I_0 \cdot \exp(-t/\tau)$ to the experimental data yields a single decay constant of τ = 540 μs at 10K. For the other modifications a deviation from this single exponential decay is observed, and an extra short component appears in the decay, being τ = 280 μs for the α-phase and the sample annealed at 1173K and τ = 160 μs for the β-modification. In both cases, the fraction of fast decay ($f_2 = (I_2\tau_2)/(I_1\tau_1 + I_2\tau_2)$) is ca. 0.75. The suppression of this second component in the decay proves that the annealing at 973 K reduces the quenching centers in the material. By contrast, higher annealing temperatures tend to have a negative effect on the internal quantum efficiency of the material. As the internal quantum efficiency of a specific transition is governed by the competition between the radiative and nonradiative decay paths, each with their own rate constant, the nonradiative decay starts to dominate if its rate constant becomes of the same order of magnitude as the intrinsic radiative decay rate. The grayish body color of the β-phase sample reveals indeed an increased absorption by defects as compared to the other samples which have a brighter body color, leading to a lower emission efficiency. The decay constant of the emission from the $^5D_1$ level is of the order of a microsecond for all four samples (Figure S4).

At room temperature (T_R), the decay of the $^5D_0$ emission of all samples is much faster as compared to the situation at 10 K. Apparently, at T_R the emission is already partially quenched. The decay constant of the $^5D_1$ emission is similar for all four samples (τ = 200 ns), whereas the decay profile of the $^5D_0$ emission differs largely. The invariance of the $^5D_1$ decay reflects an equally efficient relaxation process from the $^5D_1$ to the $^5D_0$ level for the investigated samples. Therefore, the increased $^5D_{1,2} - {}^7F_J$ emission relative to the $^5D_0$ emission of the β-phase in the steady state spectra should be linked with the fast decay of the $^5D_0$ emission. This fast decay originates from an increased probability for nonradiative decay, which is reflected in a decrease of the internal quantum efficiency of the emission from the $^5D_0$ level. Due to the 3D framework of Eu^{3+} atoms in the β-phase, the Eu ions are highly connected to each other, making energy transfer from one Eu^{3+} ion to another and subsequently to defect centers more probable. In addition, additional impurities or defects are created by elevated temperatures in the preparation phase. The combination of this more efficient transfer process and the increased number of defects results in an increase of the rate constant for the nonradiative decay paths. Given that the decay from the $^5D_0$ level is several orders of magnitude slower than from the $^5D_1$ level, the influence of the nonradiative decay rate is much larger for the $^5D_0$ level. This results in a relatively stronger reduction for the emission intensity for the transitions starting from the $^5D_0$ level, compared to those from the $^5D_1$ level.

However, it should be noted that for stoichiometric phosphors much lower quantum efficiencies are usually observed. For high Eu^{3+} concentrations, distances between Eu^{3+} atoms become so small that cross-relaxation and other energy transfer processes gain importance, resulting in strong concentration quenching and thus a reduced emission intensity. For these scheelites, however, relatively high emission intensity is found despite the high Eu^{3+} concentration. In this way, the relatively low absorption strength of the 4f-4f transitions in Eu^{3+} can be compensated to yield a reasonable absorption upon direct excitation.

3.8. Electron Energy Loss Spectroscopy. In order to pinpoint the effect of structural changes and of differences in thermal treatments on the luminescent properties, low-loss EELS spectroscopy can be applied since it is a local technique and therefore facilitates correlating spectra with certain individual crystallites or even domains. In our earlier EELS measurements performed on $Na_xEu_y(MoO_4)_z$ and $R_2(MoO_4)_3$ (R = Eu, Gd),[48,52] we determined the relation between the structure/cation distribution and the number and position of bands in the UV−vis-IR regions of the EELS energy spectrum.

EELS spectra are shown in the 150 to 1200 nm range (equivalent to 1 to 8 eV) (Figure 13), covering three different regions of the electromagnetic spectrum: ultraviolet (UV) below 380 nm (region I), visible (Vis) from 380 to 740 nm (region II), and infrared (IR) above 780 nm (Region III). All EELS spectra show a broad absorption band in region I. The positions of these broad absorption bands (~180−215 nm) are similar to the positions of the same bands (~215−240 nm) on the EELS spectra of earlier studied $Na_xEu_y(MoO_4)_z$[28] and $R_2(MoO_4)_3$ (R = Gd, Eu).[52]

In comparing the EELS spectra with the optical emission and excitation spectra, one has to keep in mind that EELS probes all interband transitions, also the optically forbidden transitions involving nondipole and transitions involving momentum transfer. As these nonoptical transitions probe a wider range

DOI: 10.1021/acs.chemmater.5b01622
Chem. Mater. 2015, 27, 5519−5530

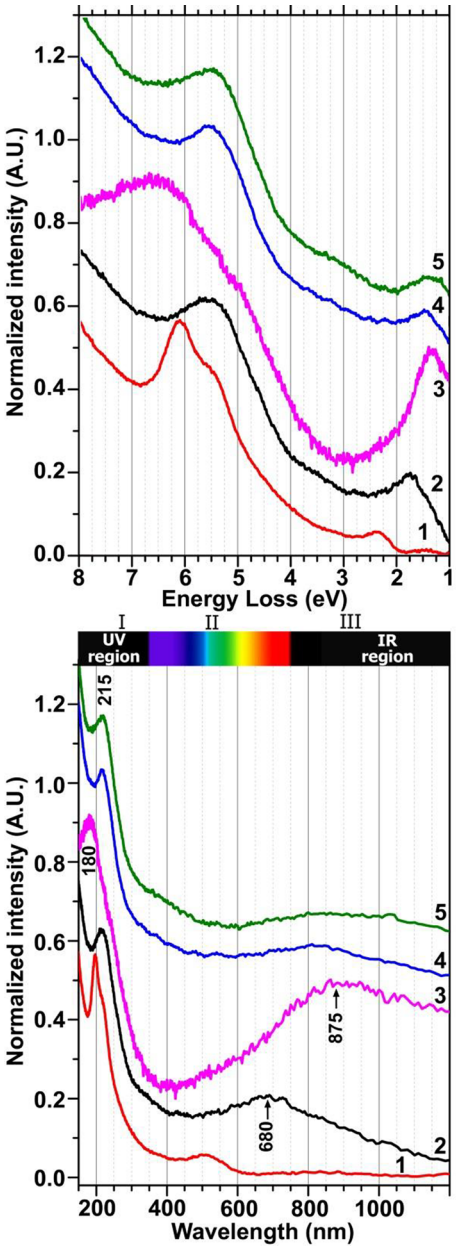

Figure 13. a) EELS spectra of K_2MoO_4 (1), α-$KEu(MoO_4)_2$ (2), and $KEu(MoO_4)_2$ annealed at 973 K (3) and 1173 K (4) followed by slow cooling to room temperature and β-$KEu(MoO_4)_2$ (5) prepared at 1203 ± 10 K followed by fast quenching to liquid nitrogen plotted as a function of energy loss. b) Same spectra plotted in wavelength scale. (I - ultraviolet region, II - visible light, and III - infrared region). Spectra are normalized in the displayed region and shifted vertically for clarity of display. Scales were matched for easy comparison with PLE and PL spectra.

of the band structure of the material, the EELS spectra contains less sharp features, but nevertheless clear differences between the different materials are apparent.

Changing the $KEu(MoO_4)_2$ structure from the anorthic α-phase to the modulated monoclinic phase during the annealing at 973 K (Table S1 of the Supporting Information) leads to a shift of the maximum from ~215 nm to ~180 nm (Figure 13). Further increase of the annealing temperature from 973 to 1173 K returns to an initial maximum value ~215 nm. Moreover the change of cooling conditions from slow cooling to liquid nitrogen quenching barely changes the EELS spectrum over the entire range of wavelengths.

Some peculiarities are observed in regions II and III of the investigated compound. As shown in Figure 13, the EELS spectrum of K_2MoO_4 is characterized by the presence of a second absorption band at ~500 nm, while the EELS spectra of $KEu(MoO_4)_2$ prepared at 973, 1173 (slow cooling), and 1203 K (quenching) do not contain clearly observed peaks in the visible and infrared regions but broad absorption bands appear around 875 nm and a shoulder in the violet-blue part of the visible range which can further be seen in the spectrum of α-$KEu(MoO_4)_2$. The EELS spectrum of α- $KEu(MoO_4)_2$ in the region from 380 to 1200 nm shows the presence of one absorption band at ~680 nm in the visible range. The position of this band is close to the positions of the same bands on the EELS spectra of earlier studied $Na_{0.286}Eu_{0.571}MoO_4$ (~735 nm)[48] and β'-$R_2(MoO_4)_3$ (R = Gd, Eu; 680–700 nm)[52] providing hints that it is related to the Eu^{3+} excitation. Thermal annealing of α-$KEu(MoO_4)_2$ and the transformation from the anorthic structure to the modulated monoclinic structure leads to a vanishing of the band at ~680 nm and the appearance of a new broad absorption band at ~875 nm which remains for both types of cooling of the β-$KEu(MoO_4)_2$. In contrast with $Na_5Eu(MoO_4)_4$[48] and both modifications of $Eu_2(MoO_4)_3$,[52] EELS spectra of all $KEu(MoO_4)_2$ samples contain no peaks associated with Eu–Eu interactions in the structure in the infrared region >1000 nm.

The band observed in the EELS spectra in the range 400–1000 nm (1–3 eV) is related to 4f-4f transitions of the Eu^{3+} ions. The 4f-4f transitions are forbidden by the Laporte selection rule but forced electric dipole and magnetic dipole transitions (called "hypersensitive transitions"[53] $|\Delta L| \leq 2$, $|\Delta J| \leq 2$, $\Delta S = 0$) are usually observed in optical excitation and emission spectra[54–56] and are at the origin of the interest of phosphors as laser or light emitters and usually seen as sharp lines. Some further excitations are optically forbidden (the ones where a small momentum transfer or spin flip is involved) but can be observed in EELS as was demonstrated in reflection EELS mode many years ago[57,58] by variation of the momentum or the collected spin, where it was demonstrated that 4f-4f transitions give rise to a large band in EELS. As we use large collection angles and much higher electron velocities as compared to reflection EELS in the experiment reported here, dipole-forbidden 4f-4f transitions are accessible. Therefore, the $^7F_0$, $^7F_1 \rightarrow {}^5D_j$ transitions are visible in EELS as well, resulting in the observed broad band.

Thus, the local low loss EELS measurements show a clear difference between the anorthic α-$KEu(MoO_4)_2$ and the modulated monoclinic β-phase and an influence of the synthesis conditions on the band positions.

4. CONCLUSION

The α- and β-polymorphs of $KEu(MoO_4)_2$ were synthesized by a solid state method. PXRD study confirmed the existence of only two polymorphic forms at annealing temperature range 923–1203 K and ambient pressure: a low temperature anorthic α-phase and a monoclinic high temperature β-phase with an incommensurately modulated structure. The structures of both $KEu(MoO_4)_2$ polymorphs were studied using different transmission electron microscopy techniques and refined from synchrotron powder X-ray diffraction data using a (3+1)D formalism. In both cases the modulation arises due to Eu/K cation ordering at the A site: the formation of a 2D Eu^{3+}

DOI: 10.1021/acs.chemmater.5b01622
Chem. Mater. 2015, 27, 5519–5530

network is characteristic for the α-phase, while a 3D Eu^{3+}-framework is observed for the β-phase. The most intense luminescence provided by Eu^{3+} is observed in the case of the minimum size of the Eu^{3+} clusters (isolated from other Eu^{3+} ions).[59] The higher the concentration of the smallest clusters, the better luminescence properties can be observed.[47] The present report shows that a layered network of Eu^{3+} ions results in better luminescence properties in comparison to a 3D framework of Eu^{3+} ions. Hence, the Eu^{3+}-framework and the size of the Eu^{3+} clusters affect the luminescence properties of the Eu^{3+} containing compounds.

■ ASSOCIATED CONTENT

Supporting Information

The Supporting Information is available free of charge on the ACS Publications website at DOI: 10.1021/acs.chemmater.5b01622.

Tables S1−S6 and Figures S1−S4 (PDF)

■ AUTHOR INFORMATION

Corresponding Author

*Phone: 32-32653245. Fax: 32-32653257. E-mail: joke.hadermann@uantwerpen.be.

Notes

The authors declare no competing financial interest.

■ ACKNOWLEDGMENTS

This research was supported by FWO (project G039211N), Flanders Research Foundation. V.A.M. acknowledges financial support of the Russian Foundation for Basic Research (Grants 12-03-00124 and 15-03-07741). J.V. and N.G. are grateful for support from the European Research Council under an ERC starting grant No. 278510 VORTEX. J.V. also acknowledges FWO project G.0044.13N.

■ REFERENCES

(1) Shur, M. S.; Zukauskas, A. Solid-state lighting: Toward superior illumination. *Proc. IEEE* **2005**, *93*, 1691−1703.

(2) Yam, F. K.; Hassan, Z. Innovative advances in LED technology. *Microelectron. J.* **2005**, *36*, 129−137.

(3) Kim, T.; Kang, S. Potential red phosphor for UV-white LED device. *J. Lumin.* **2007**, *122*−*123*, 964−966.

(4) Hwang, K.-S.; Jeon, Y.-S.; Hwangbo, S.; Kim, J.-T. Red-emitting $LiEuW_2O_8$ phosphor for white emitting diodes prepared by sol−gel process. *Opt. Appl.* **2009**, *39*, 375−383.

(5) Yan, B.; Wu, J.-H. $NaY(MoO_4)_2$:Eu^{3+} and $NaY_{0.9}Bi_{0.1}(MoO_4)_2$:$Eu^{3+}$ submicrometer phosphors: Hydrothermal synthesis assisted by room temperature-solid state reaction, microstructure and photoluminescence. *Mater. Chem. Phys.* **2009**, *116*, 67−71.

(6) Haque, Md. M.; Lee, H.-I.; Kim, D.-K. Luminescent properties of Eu^{3+}-activated molybdate-based novel red-emitting phosphors for LEDs. *J. Alloys Compd.* **2009**, *481*, 792−796.

(7) Guo, C.; Gao, F.; Xu, Y.; Liang, L.; Shi, F. G.; Yan, B. Efficient red phosphors $Na_5Ln(MoO_4)_4$:Eu^{3+} (Ln = La, Gd and Y) for white LEDs. *J. Phys. D: Appl. Phys.* **2009**, *42*, 095407.

(8) Meert, K. W.; Morozov, V. A.; Abakumov, A. M.; Hadermann, J.; Poelman, D.; Smet, P. F. Energy transfer in Eu^{3+} doped scheelites: use as thermographic phosphor. *Opt. Express* **2014**, *22*, A961−A972.

(9) Shao, Q.; Li, H.; Wu, K.; Dong, Y.; Jiang, J. Photoluminescence studies of red-emitting $NaEu(WO_4)_2$ as a near-UV or blue convertible phosphor. *J. Lumin.* **2009**, *129*, 879−883.

(10) Yi, L.; Zhou, L.; Wang, Z.; Sun, J.; Gong, F.; Wan, W.; Wang, W. $KGd(MoO_4)_2$:Eu^{3+} as a promising red phosphor for light-emitting diode application. *Curr. Appl. Phys.* **2010**, *10*, 208−213.

(11) Trunov, V. K.; Efremov, V. A.; Velikodnii, Yu. A. *Crystallography and properties of double molybdates and tungstenates*; Nauka: Leningrad, 1986 (in Russian).

(12) Evdokimov, A. A.; Efremov, V. A.; Trunov, V. K. *Compounds of the rare earth elements*; Nauka: Moscow, 1991 (in Russian).

(13) Guo, C.; Wang, S.; Chen, T.; Liang, L.; Xu, Y. Preparation of phosphors $AEu(MoO_4)_2$ (A = Li, Na, K and Ag) by sol-gel method. *Appl. Phys. A: Mater. Sci. Process.* **2009**, *94*, 365−371.

(14) Benoît, G.; Véronique, J.; Arnaud, A.; Alain, G. *Solid State Sci.* **2011**, *13*, 460−467.

(15) Huang, X.; Wang, G. Growth and optical characteristics of Er^{3+}:$LiLa(MoO_4)_2$ crystal. *J. Alloys Compd.* **2009**, *475*, 693−697.

(16) Huang, X.; Wang, G. Growth, thermal and spectroscopic characteristics of Nd^{3+}:$LiGd(MoO_4)_2$ crystal. *J. Phys. D: Appl. Phys.* **2008**, *41*, 225401.

(17) Pang, Z. L.; Zhang, L. Z.; Lin, Z. B.; Wang, G. F. Growth and spectroscopic characterisation of Tm^{3+}/Yb^{3+} codoped $LiGd(MoO_4)_2$ crystal. *Mater. Res. Innovations* **2008**, *12*, 30−34.

(18) Zhao, D.; Li, F.; Chen, W.; Zhang, H. Scheelite-type $NaEr(MoO_4)_2$. *Acta Crystallogr., Sect. E: Struct. Rep. Online* **2010**, *66*, i36.

(19) Kuz'micheva, G. M.; Lis, D. A.; Subbotin, K. A.; Rybakov, V. B.; Zharikov, E. V. Growth and structural X-ray investigations of scheelite-like single crystals Er, Ce:$NaLa(MoO_4)_2$ and Yb:$NaGd(WO_4)_2$. *J. Cryst. Growth* **2005**, *275*, e1835−e1842.

(20) Voron'ko, Y. K.; Subbotin, K. A.; Shukshin, V. E.; Lis, D. A.; Ushakov, S. N.; Popov, A.; Zharikov, E. V. Growth and spectroscopic investigations of Yb^{3+}-doped $NaGd(MoO_4)_2$ and $NaLa(MoO_4)_2$—new promising laser crystals. *Opt. Mater.* **2006**, *29*, 246−252.

(21) Wu, J.; Yan, B. Room-temperature solid-state reaction behavior, hydrothermal crystallization and physical characterization of $NaRE(MoO_4)_2$, and $Na_5Lu(MoO_4)_4$ compounds. *J. Am. Ceram. Soc.* **2010**, *93*, 2188−2194.

(22) Sleight, A. W.; Aykan, K.; Rogers, D. B. New nonstoichiometric molybdate, tungstate, and vanadate catalysts with the scheelite-type structure. *J. Solid State Chem.* **1975**, *13*, 231−236.

(23) Rath, M.; Müller-Buschbaum, Hk. Zur kristallstruktur von silber-lanthanoid-oxomolybdaten $AgLnMo_2O_8$: einkristalluntersuchungen an $AgSmMo_2O_8$ und $AgYbMo_2O_8$ mit einer notiz über mikrokristallines material für Ln = Y, La. *J. Alloys Compd.* **1993**, *198*, 193−196.

(24) Shi, F.; Meng, J.; Ren, Y. Preparation structure and physical properties of new silver lanthanide molybdenum oxides [$AgLnMo_2O_8$, (Ln = La-Nd and Sm)]. *Mater. Res. Bull.* **1995**, *30*, 1401−1405.

(25) Taira, N.; Hinatsu, Y. Magnetic properties of silver lanthanide molybdates $AgLnMo_2O_8$ (Ln = lanthanide). *J. Mater. Chem.* **2002**, *12*, 148−152.

(26) Hanuza, J.; Benzar, A.; Haznar, A.; Maczka, M.; Pietraszko, A.; van der Maas, J. H. Structure and vibrational dynamics of tetragonal $NaBi(WO_4)_2$ scheelite crystal. *Vib. Spectrosc.* **1996**, *12*, 25−36.

(27) Volkov, V.; Cascales, C.; Kling, A.; Zaldo, C. Growth, structure, and evaluation of laser properties of $LiYb(MoO_4)_2$ single crystal. *Chem. Mater.* **2005**, *17*, 291−300.

(28) Cascales, C.; Serrano, M. D.; Esteban-Betegón, F.; Zaldo, C.; Peters, R.; Petermann, K.; Huber, G.; Ackermann, L.; Rytz, D.; Dupre, C.; Rico, M.; Liu, J.; Griebner, U.; Petrov, V. Structural, spectroscopic, and tunable laser properties of Yb^{3+}-doped $NaGd(WO_4)_2$. *Phys. Rev. B: Condens. Matter Mater. Phys.* **2006**, *74*, 174114.

(29) Klevtsova, R. F.; Borisov, S. V. X-ray diffraction studies of $KY(MoO_4)_2$ double molybdate. *Dokl. Acad. Nauk SSSR* **1967**, *177*, 1333−136 (in Russian).

(30) *Powder Diffraction File*, Cards 32-0804, 33-1035 and 51-1846 JCPDS; International Centre for Diffraction Data, 1601 Park Lane, Swarthmore, PA 19081.

(31) Cavalli, E.; Meschini, C.; Toncelli, A.; Tonelli, M.; Bettinelli, M. Optical spectroscopy of Tm^{3+} doped in $KLa(MoO_4)_2$ crystals. *J. Phys. Chem. Solids* **1997**, *58*, 587−595.

DOI: 10.1021/acs.chemmater.5b01622
Chem. Mater. 2015, 27, 5519−5530

(32) Potapova, O. G.; Protasova, V. I.; Kharchenko, L. Yu. X-ray diffraction study of $KLa(MoO_4)_2$ crystals prepared by hydrothermal method. *Zh. Neorg. Khim.* **1987**, *32*, 2933−2938 (in Russian); *Russ. J. Inorg. Chem. (Transl. Zh. Neorg. Khim.)* **1987**, *32*, 1703 (in English..
(33) Klevtsov, P. V.; Kozeeva, L. P.; Pavlyuk, A. A. Polymorphism and crystallization of potassium-rare earth element molybdates $KLn(MoO_4)_2$ (Ln = La, Ce, Pr and Nd). *Crystallogr. Rep.* **1975**, *20*, 1216−1220 (in Russian).
(34) Morozov, V. A.; Arakcheeva, A. V.; Chapuis, G.; Guiblin, N.; Rossell, M. D.; Van Tendeloo, G. $KNd(MoO_4)_2$: A New Incommensurate Modulated Structure in the Scheelite Family. *Chem. Mater.* **2006**, *18*, 4075−4082.
(35) Arakcheeva, A.; Pattison, P.; Chapuis, G.; Rossell, M.; Filaretov, A.; Morozov, V.; Van Tendeloo, G. $KSm(MoO_4)_2$, an incommensurately modulated and partially disordered scheelite-like structure. *Acta Crystallogr., Sect. B: Struct. Sci.* **2008**, *64*, 160−171.
(36) Klevtsova, R. F.; Kozeeva, L. P.; Klevtsov, P. V. Preparation and structure of the crystals of potassium-europium molybdate $KEu(MoO_4)_2$. *Crystallogr. Rep.* **1974**, *19*, 89−94 (in Russian).
(37) Klevtsov, P. V.; Kozeeva, L. P. The crystalline modifications of double molybdates of potassium with samarium, europium and gadolinium, $KLn(MoO_4)_2$. *Crystallogr. Rep.* **1976**, *21*, 316−321 (in Russian).
(38) Mokhosoev, M. B.; Getman, E. I.; Alekseev, F. P. Double molybdates of alkali and rare earth elements $MeLn(MoO_4)_2$. *Dokl. Akad. Nauk SSSR* **1969**, *185*, 361−362 (in Russian).
(39) Spitsin, V. I.; Trunov, V. K. New data on the double tungstates and molybdates $MeLn(AO_4)_2$ composition. *Dokl. Akad. Nauk SSSR* **1969**, *185*, 854−855 (in Russian).
(40) Macalik, L.; Hanuza, J.; Macalik, B.; Strek, W.; Legendziewicz, J. Comparative studies of optical properties of Eu(III) in $KEu(MoO_4)_2$ and $KEu(WO_4)_2$ crystals. *Eur. J. Solid State Inorg. Chem.* **1996**, *33*, 397−410.
(41) Le Bail, A.; Duroy, H.; Fourquet, J. L. Ab-initio structure determination of $LiSbWO_6$ by X-ray powder diffraction. *Mater. Res. Bull.* **1988**, *23*, 447−452.
(42) Petrícek, V.; Dusek, M.; Palatinus, L. *JANA2000: the crystallographic computing system*; Institute of Physics: Praha, Czech Republic, 2000.
(43) Dusek, M.; Petrícek, V.; Wunschel, M.; Dinnebier, R. E.; Van Smaalen, S. Refinement of modulated structures against X-ray powder diffraction data with *JANA2000*. *J. Appl. Crystallogr.* **2001**, *34*, 398−404.
(44) Brandenburg, K. *DIAMOND, Version. 2.1c*; Crystal Impact GbR; Bonn, Germany, 1999.
(45) Van Smaalen, S.; Campbell, B. J.; Stokes, H. T. Equivalence of superspace groups, Acta Crystallogr. *Acta Crystallogr., Sect. A: Found. Crystallogr.* **2013**, *69*, 75−90.
(46) Abakumov, A. M.; Morozov, V. A.; Tsirlin, A. A.; Verbeeck, J.; Hadermann, J. Cation ordering and flexibility of the BO_4^{2-} tetrahedra in incommensurately modulated $CaEu_2(BO_4)_4$ (B = Mo, W) Scheelites. *Inorg. Chem.* **2014**, *53*, 9407−9415.
(47) Arakcheeva, A.; Logvinovich, D.; Chapuis, G.; Morozov, V.; Eliseeva, S. V.; Bunzli, J.-C. G.; Pattison, P. The luminescence of $Na_xEu^{3+}_{(2-x)/3}MoO_4$ scheelites depends on the number of Eu-clusters occurring in their incommensurately modulated structure. *Chem. Sci.* **2012**, *3*, 384−390.
(48) Morozov, V. A.; Lazoryak, B. I.; Shmurak, S. Z.; Kiselev, A. P.; Lebedev, O. I.; Gauquelin, N.; Verbeeck, J.; Hadermann, J.; Van Tendeloo, G. Influence of the structure on the properties of $Na_xEu_y(MoO_4)_z$ red phosphors. *Chem. Mater.* **2014**, *26*, 3238−3248.
(49) Zhang, H.-J.; Fu, L.; Wang, C.-P.; Fu, H. F.; Xie, W. G. Crystal structure of Scheelite-type potassium cerium bis(tetraoxomolybdate-(VI)), $KCe(MoO_4)_2$. *Z. Kristallogr. - New Cryst. Struct.* **2014**, *229*, 191−192.
(50) Basovich, O. M.; Khaikina, E. G.; Solodovnikov, S. F.; Tsyrenova, G. D. Phase formation in the systems Li_2MoO_4−K_2MoO_4−$Ln_2(MoO_4)_3$ (Ln = La, Nd, Dy, Er) and properties of triple molybdates $LiKLn_2(MoO_4)_4$. *J. Solid State Chem.* **2005**, *178*, 1580−1588.
(51) Tanner, P. Some misconceptions concerning the electronic spectra of tri-positive europium and cerium. *Chem. Soc. Rev.* **2013**, *42*, 5090−5101.
(52) Morozov, V. A.; Raskina, M. V.; Lazoryak, B. I.; Meert, K. W.; Korthout, K.; Smet, P. F.; Poelman, D.; Gauquelin, N.; Verbeeck, J.; Abakumov, A. M.; Hadermann, J. Crystal structure and luminescent properties of $R_{2-x}Eu_x(MoO_4)_3$ (R = Gd, Sm) red phosphors. *Chem. Mater.* **2014**, *26*, 7124−7136.
(53) Jørgensen, C. K.; Judd, B. R. Hypersensitive pseudoquadrupole transitions in lanthanides. *Mol. Phys.* **1964**, *8*, 281−290.
(54) Carnall, W. T.; Goodman, G. L.; Rajnak, K.; Rana, R. S. A systematic analysis of the spectra of the lanthanides doped into single crystal LaF_3. *J. Chem. Phys.* **1989**, *90*, 3443−3457.
(55) Dorenbos, P. A. Review on How Lanthanide Impurity Levels Change with Chemistry and Structure of Inorganic Compounds. *ECS J. Solid State Sci. Technol.* **2012**, *2*, R3001−R3011.
(56) Malta, O. L.; Carlos, L. D. Intensities of 4f-4f transitions in glass materials. *Quim. Nova* **2003**, *26*, 889−895.
(57) Fromme, B.; Bocatius, V.; Kisker, E. Electron exchange in the f-f excitations of EuO. *Phys. Rev. B: Condens. Matter Mater. Phys.* **2001**, *64*, 1−8.
(58) Gorschlüter, A.; Stiller, R.; Merz, H. Dipole forbidden f-f excitation in ytterbium oxide. *Surface Science Letters* **1991**, *251*−*252*, A324.
(59) Ananias, D.; Kostova, M.; Paz, F. A. A.; Neto, A. N. C.; DeMoura, R. T.; Malta, O. L.; Carlos, L. D.; Rocha, J. Molecule-like Eu^{3+}-dimers embedded in an extended system exhibit unique photoluminescence properties. *J. Am. Chem. Soc.* **2009**, *131*, 8620−8626.

DOI: 10.1021/acs.chemmater.5b01622
Chem. Mater. 2015, 27, 5519−5530